Available online at www.sciencedirect.com
ScienceDirect
Sensors and Actuators A 132 (2006) 452–459
SENSORS AND ACTUATORS A PHYSICAL
www.elsevier.com/locate/sna

Micromachined bolometers on polyimide

Aamer Mahmood, Donald P. Butler, Zeynep Çelik-Butler *

Department of Electrical Engineering, University of Texas at Arlington, Nanofab Center, P.O. Box 19072, Arlington, TX 76019, United States

Received 12 August 2005; received in revised form 8 March 2006; accepted 8 March 2006
Available online 18 April 2006

Abstract

This paper presents design, fabrication and measured performance parameters of micromachined infrared detectors on polyimide substrates. The detectors are of bolometer type made of semiconducting yttrium–barium–copper oxide (YBCO) as the thermometer material and are built on a 40–50 μm-thick layer of polyimide (PI5878G) that serves as a flexible substrate. A thin film of Si_3N_4 supports the detectors. Surface micromachining is used to isolate the detectors and the supporting nitride layer from the substrate. Despite being supported by a layer of Si_3N_4, an average thermal conductivity of 5.61×10^{-7} W/K, comparable to self-supporting devices on flexible substrates has been measured. This opens the possibility of placing such flexible sensors on micromachined membranes, integrated with other functions such as pressure sensing to build "Smart Skin." Room-temperature responsivity of 7.4×10^3 V/W and detectivity of 6.6×10^5 cm Hz$^{1/2}$/W were demonstrated on 40 μm × 40 μm microbolometers. The effect of substrate heating was also investigated and was found not to cause cross talk between the pixels. If these sensors are to be used as part of multi-functional, flexible sensor systems, device-level vacuum packaging is necessary. This was investigated using computer simulations for structural analysis and found to be feasible.
© 2006 Elsevier B.V. All rights reserved.

Keywords: Microbolometers; Flexible sensors; Thermal sensors; Wafer-level packaging; Micromachining; Finite-element analysis

1. Introduction

The coalescence of integrated electronics and MEMS has made the goal of system-on-a-chip – a single package containing sensors, actuators and associated electronic circuitry in one chip – realizable. Flexible substrates facilitate conformal electronics, enabling foldable systems-on-a-chip, made of sensors, electronics and actuators, with possible applications as electronic fabrics, smart tags and conformal sensor arrays among others in the fields of defense, medicine, industrial monitoring and testing. Microbolometers on flexible substrates are part of a strategic goal of making a "smart skin"—a flexible substrate housing a plethora of sensor systems for measuring parameters like temperature, moisture, pressure, fluid flow and acceleration. Typically, however, the performance optimization of each type of sensor would put contradicting requirements on design parameters. For example, if pressure and thermal sensors are to be integrated on a single micromachined bridge, as would be required in case of the "smart skin", the mass, dimensions, material properties (thermal conductivity, specific heat etc.) of the bridge structure need to be optimized as a shuttle mass for the pressure sensors and as a support with low thermal conductivity and mass for the thermal detectors. Therefore, it is essential to investigate the performance of such flexible bolometers on a micromachined membrane. Similarly, if these systems were to be used autonomously, self-packaging is necessary to maintain flexibility. Consequently, computer simulations are performed here to analyze the feasibility of device-level vacuum packaging of these detectors.

Different materials used as bolometers include vanadium oxide VO_x [1–10], amorphous Si [11–15], doped poly Si [16,17], and poly Si–Ge alloys [17–19]. Thin film metals like Ti [20,21], Nb [4,22] and Pt [23,24] have also been reported. In this work, the radiation sensitive material used is the polycrystalline form of semiconducting $YBa_2Cu_3O_{6+x}$ (referred to as YBCO). The structural, electrical and optical properties of the material vary with the oxygen content x [25,26]. For $0.3 \leq x \leq 0.5$, $YBa_2Cu_3O_{6+x}$ behaves as a semiconductor and in crystalline form it is tetragonal. Amorphous YBCO thin films deposited on Si wafers with a buffer layer have exhibited a temperature coefficient of resistance (TCR) of $\sim -3.1\%\,K^{-1}$. YBCO can be rf-sputtered from a target at room temperature to yield thin

* Corresponding author. Tel.: +1 817 272 1309; fax: +1 817 272 7458.
E-mail address: zbutler@uta.edu (Z. Çelik-Butler).

0924-4247/$ – see front matter © 2006 Elsevier B.V. All rights reserved.
doi:10.1016/j.sna.2006.03.006

films for use as microbolometers [25–32]. The ability of low-temperature deposition makes this material especially suitable as a sensor material on polyimides, majority of which have stringent thermal budgets.

Work on YBCO microbolometers started on rigid Si substrates [29–32], which was followed by microbolometers on flexible substrates. The first generation devices on flexible substrates were made on prefabricated sheets of polyimide, Kapton®, using a Si wafer as carrier during the fabrication [26]. This was problematic in that the polyimide substrate could not be kept planar on the silicon due to the formation of bubbles and the difference in thermal coefficients of expansion between the polyimide and the subsequent layers. The next generation of detectors was made by using spin-on polyimide layers (such as PI5878G from HD Microsystems), which were subsequently cured to form the flexible substrate. Again, Si wafers were used as a carrier. The completed devices were then peeled off the carrier to obtain the flexible detectors arrays [32]. The spin-on polyimide is fully CMOS compatible in that it is resistant to typical process chemicals. It has a glass transition temperature (T_g) of ∼400 °C, providing ample thermal budget downstream in the fabrication. Moreover, it poses no adhesion problems for layers deposited on it.

To achieve low thermal conductance and hence high responsivity, bolometers are generally vacuum-packaged, which constitutes a large fraction of the overall cost of the sensor systems. Wafer- and device-level packaging techniques have been proposed to cut cost and improve reliability [33,34]. A new device-level vacuum packaging process that envisages a vacuum cavity created around the microbolometer during fabrication is investigated. The detector is embedded in a sacrificial polyimide. A cavity wall/optical window combination is created using an optically transparent material. Openings in the optical window can be used to remove all the sacrificial material around and underneath the detector by conventional micromachining techniques. The openings in the optical window can then be sealed shut in vacuum to yield a vacuum cavity "package". This technique is fully compatible with current CMOS fabrication techniques and can be used for flexible substrate microbolometers. A vacuum cavity containing a microbolometer has been simulated using finite-element analysis based CoventorWare®. The flexible substrate hosting the cavity was deflected up to a radius of 2 mm. The stresses produced in the cavity materials were seen to remain in the linear/elastic region up to a radius of ∼10 mm proving the feasibility of this fabrication scheme.

2. Detector fabrication

All depositions in the fabrication were done using 3-in. targets in an rf-magnetron sputter system in a pure Ar environment of 10 m Torr pressure. First, 4000 Å of Si_3N_4 was sputtered on to the Si wafer for passivation and improved adhesion of the subsequent polyimide layer. This was followed by spin-coating liquid polyimide PI5878G onto the wafer, which was repeated five times. The polyimide-coated wafer was then loaded into an oven at 110–115 °C. The oven temperature was gradually ramped to 275 °C, where the polyimide was cured for 5 h to

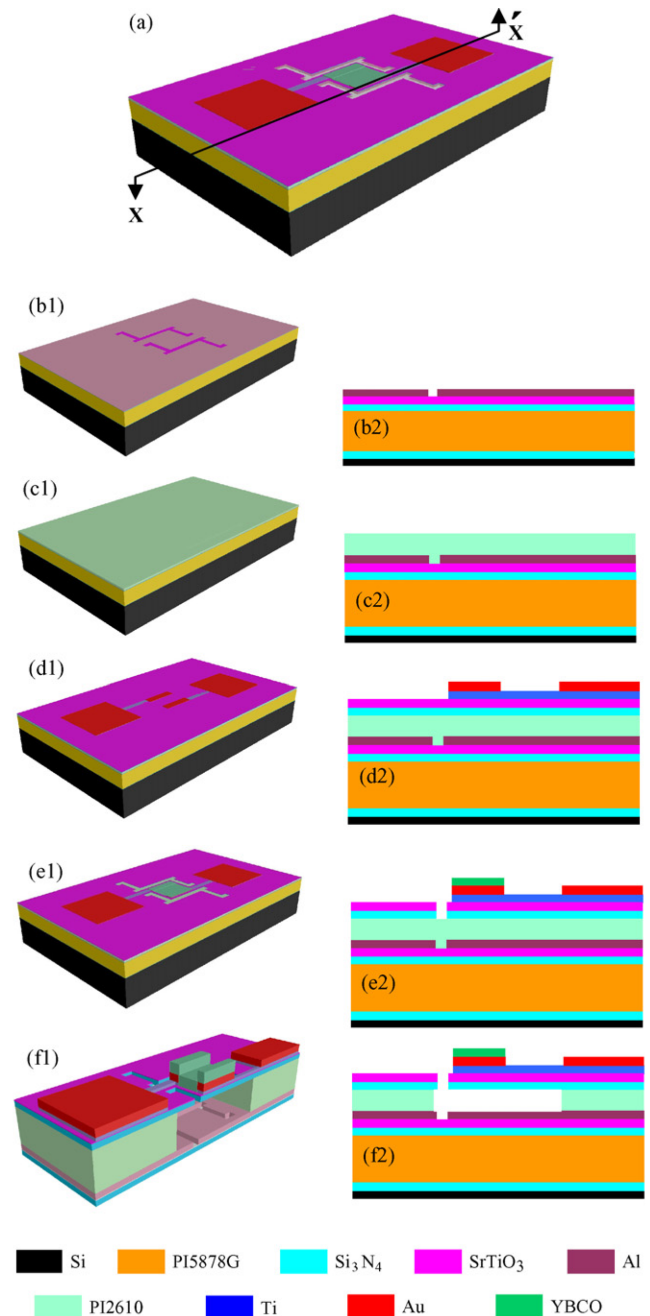

Fig. 1. Fabrication steps of microbolometers on flexible substrate. (a) CoventorWare® generated model of a completed device, (b1) model showing Al layer with open trenches, (b2) cross section view of slice at *XX′* showing trench opening in Al layer, (c1) model showing sacrificial polyimide, (c2) cross section view of slice at *XX′* showing sacrificial polyimide, (d1) model showing patterned Ti arms and Au pads above support membrane, (d2) cross section view of slice at *XX′* showing Ti arm and Au pads above support membrane, (e1) model showing YBCO detector in place, (e2) cross section view of slice at *XX′* showing YBCO detector above Au contact pad, (f1) model sectioned at *XX′* and magnified 20X along the height of the detector to show cavity and support details. The carrier Si wafer and PI5878G have been suppressed in this figure, (f2) cross section view of slice at *XX′* showing micromachined cavity beneath the support layer (Dimensions not to scale).

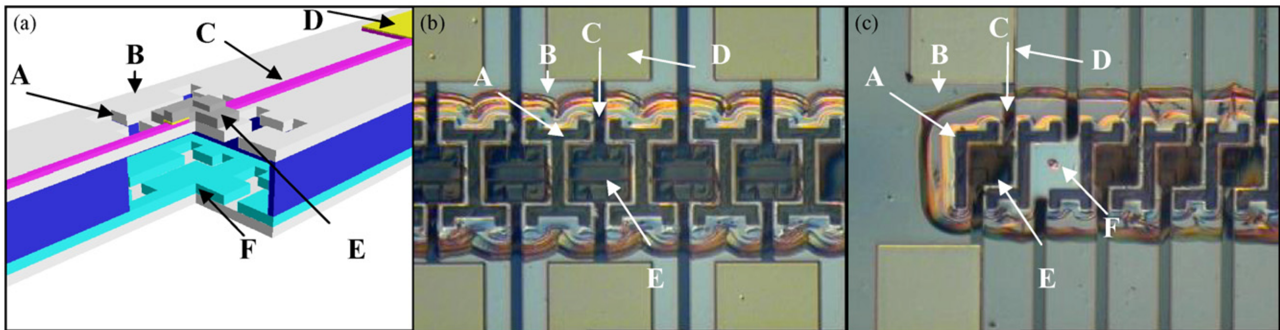

Fig. 2. Completed microbolometers on a flexible substrate showing (A) a trench in the supporting Si_3N_4 layer, (B) supporting Si_3N_4 layer, (C) Ti arm, (D) Au bond pad, (E) YBCO pixel and (F) Al reflecting mirror in; (a) cutaway of a CoventorWare® model detector pixel. The micromachined cavity under the detector can be seen; (b) Array of 60 μm × 60 μm microbolometers under a microscope, showing the extent of lateral micromachining of sacrificial PI2610 after 10 h of ashing, (c) array of 40 μm × 40 μm detectors after 10 h of ashing. The second pixel from the left has been removed and shows Al reflector surface without polyimide.

yield a final thickness of 40 μm. The polyimide was then coated with another layer of sputtered Si_3N_4. This layer serves as a passivation layer and also promotes adhesion between the polyimide and the subsequent layers sputtered during fabrication. The nitride is resistant to the wet etchants used in subsequent processing steps. To provide protection from dry etchants, a 500 Å layer of $SrTiO_3$ was sputtered. Fabrication steps up to this point are similar to those used for self-supporting micromachined microbolometers on flexible substrates reported earlier [32]. Subsequent fabrication steps are different since unlike self-supporting devices reported in Ref. [32], the current geometry employs a support layer to hold up the bolometers. A 4000 Å layer of Al was then deposited and patterned to form a reflecting mirror as part of a resonant cavity beneath the detector to improve absorption of radiation by the bolometer. The Al layer was patterned in the shape of subsequently used trenches for the sole purpose of facilitating alignment in following photolithography steps (Fig. 1(b)). PI2610 was subsequently spun on to form the sacrificial layer. After curing, the final sacrificial polyimide thickness was 0.5 μm (Fig. 1(c)). A 4000 Å thick layer of Si_3N_4 was then sputtered onto the polyimide followed by 500 Å of $SrTiO_3$ layer. A 1500 Å layer of Ti was used as the electrode material, followed by deposition and patterning of 750 Å of Au as bonding pads as well as contacts between the detector material and the electrodes. Ti was used due its relatively low thermal conductivity among conductors. Ti was then patterned by dry etching in CF_4:O_2, forming the electrode arms between the aforementioned Au pads and contacts (Fig. 1(d)). The last deposition in the fabrication process was 3600 Å of YBCO, patterned to yield the detector pixels (thermistors).

Surface micromachining was performed to remove the sacrificial layer, thus releasing the Si_3N_4 bridge supporting the detectors. Trenches were opened around each pixel in the $SrTiO_3$. This exposed the underlying layer of Si_3N_4. The wafer was put in a reactive ion etcher and the exposed nitride was dry etched. Nitride was thus removed in the trench area exposing the underlying sacrificial polyimide PI2610 (Fig. 1(e)). The sacrificial polyimide was removed by multiple steps of 10 min of oxygen ashing, followed by 10 min of cooling (Fig. 1(f)). It had been observed that heating caused by continuous ashing for long periods of time produces thermal stresses in the nitride layer supporting the detector. The cumulative ashing time was approximately 10 h. At this stage, it was seen that the PI2610 beneath the smaller 40 μm × 40 μm pixels was removed completely (Fig. 2(c)). The polyimide can be peeled off the host wafer to yield sensors on a flexible substrate.

The cutaway model of the finished structure together with the optical photos of 1 × 10 arrays are shown in Fig. 2. Different detector sizes and trench geometries are also evident.

3. Detector characterization

Electrical and optical characterization of the packaged and bonded devices was carried out. Results presented here are generally for the 40 μm × 40 μm devices unless otherwise specified. The dc resistance at 301 K was measured to be ∼3.76 MΩ. Resistance of the device was measured from 240 to 320 K (Fig. 3) and the temperature coefficient of resistance $\mathrm{TCR} = \alpha = (1/R)(\mathrm{d}R/\mathrm{d}T)$, was calculated. A TCR of $-2.63\%\ \mathrm{K}^{-1}$ at 301 K was measured. The resistance of the device varied according to the Arrhenius relation $R(T) = R_0 \exp(E_a/kT)$. The

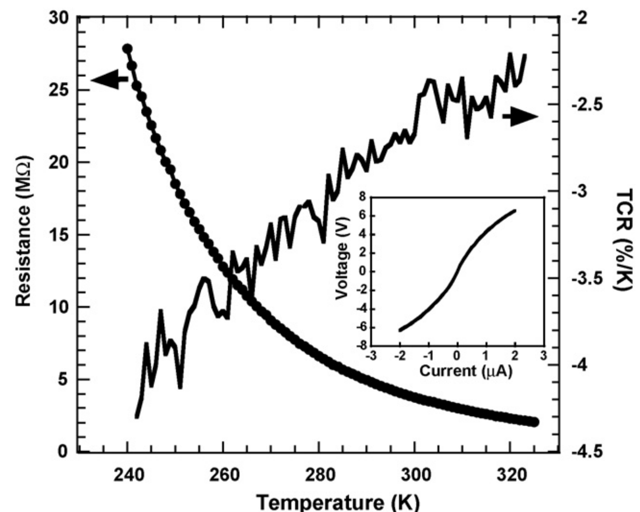

Fig. 3. Device resistance as a function of temperature and temperature coefficient of resistance. Effect of Joule heating: non-linear VI characteristics (*inset*).

values of $R_0 = 1341\,\Omega$ and the activation energy $E_a = 0.21$ eV were determined by plotting ln (R) versus $1/kT$.

The thermal conductivity of the detector to the substrate G_{th}, is a measure of the thermal isolation of the device and thus, of the extent of micromachining. Thermal conductance was measured using the Joule heating method. The detector was placed in a cryostat at room temperature and evacuated to 50 mT. The bias current I_b was swept from $-2\,\mu$A to $2\,\mu$A in increments of 100 nA and the voltage across the device measured using an HP4155B semiconductor parameter analyzer. The non-linear VI curve shows the effect of Joule heating (Fig. 3 *inset*). The effective thermal conductance G_{eff} depends on the thermal conductance G_{th}, the radiative conductance G_{rad} and the heating effect of the biasing current $P_I = VI = I_b^2 R(T)$:

$$G_{eff} = G_{th} + G_{rad} - \alpha P_I \quad (1)$$

The effective conductance is related to the temperature T and the non-linear resistance of the device as:

$$G_{eff}(T) = \frac{P_I}{\Delta T} = \frac{I_b^2 R(T)}{(T - T_0)} \quad (2)$$

where T_0 is the ambient temperature of the substrate (the heat sink). In the current geometry, G_{rad} is negligibly small. It is expressed as:

$$G_{rad} \cong 8\varepsilon A_d \sigma T_0^3 \quad (3)$$

where ε is the device emissivity and is assumed equal to the device absorption η at all wavelengths, A_d is the area of the detector and σ is the Stefan–Boltzmann constant. The dependence of the thermal conductance on the Joule heating, the non-linear resistance and TCR of the device was investigated by calculating G_{eff} and G_{th} using Eqs. (1) and (2) over the entire bias range from $-2\,\mu$A to $2\,\mu$A. The mean room temperature G_{th} was calculated to be 5.61×10^{-7} W/K with a standard deviation of 3.63×10^{-7} W/K, which is comparable to those reported earlier [32]. Similarly sized, non-micromachined devices in full contact with the substrate have a thermal conductance an order of magnitude higher [32]. Fig. 4 shows the resistance of the device as a function of the dissipated power. Measured as well as theoretical data are shown. The theoretical device resistance was calculated from the measured mean thermal conductance $\bar{G}_{th}$, using $G_{eff} = \bar{G}_{th} + G_{rad} - \alpha P_I$, and the Arrhenius relation.

The optical characterization was done using a blackbody IR source kept at 900 °C. The detector was biased from 136 nA to 970 nA. The device output was measured by a dynamic signal analyzer through a low noise preamplifier. For calibration purposes, an Oriel 70124 pyroelectric detector with a responsivity of 1000 V/W was used. The device was mounted inside a cryostat and the measurements were made in air as well as in vacuum with the cryostat evacuated to ~100 m Torr pressure. A chopper was used to modulate the infrared signal incident on the detector. Fig. 5 shows a typical signal spectrum. The device had a maximum voltage responsivity R_V of 9.2×10^2 V/W and 7.4×10^3 V/W in air and vacuum, respectively. The expression for the voltage responsivity is $R_v = \eta\alpha R I_b / G_{th}(1 + \omega^2\tau_{th}^2)^{1/2}$

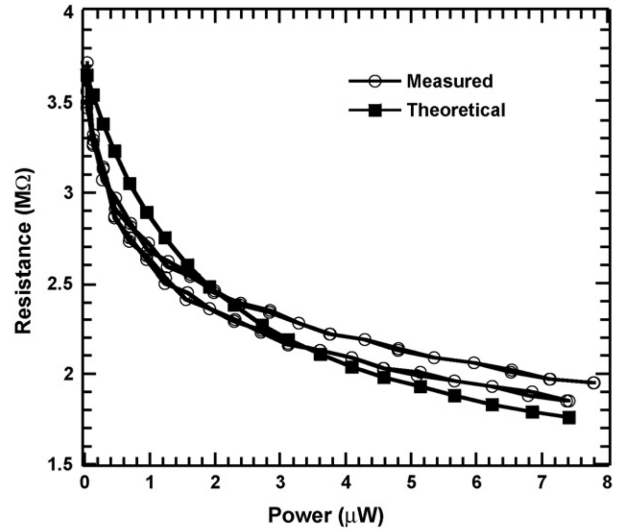

Fig. 4. Measured and theoretical resistance of the device resistance. The theoretical resistance was calculated using the mean calculated $G_{th} = 5.61 \times 10^{-7}$ W/K.

[35], where η is the optical absorption coefficient of the thermometer, ω is the angular modulation frequency of the incident IR radiation and τ_{th} is the thermal response time of the detector $\tau_{th} = C_{th}/G_{th}$, i.e., the ratio of the thermal capacitance to the thermal conductance of the microbolometer. The fact that there is an appreciable improvement in the detector responsivity with evacuation of air points to good thermal isolation achieved between the detector and the substrate by micromachining. In addition to the signal at different chopper frequencies, noise at these frequencies was also measured (Fig. 5), which was used to calculate the specific detectivity defined as $D^* = R_v\sqrt{A\Delta f}/\Delta V_n$ [35]. Here, A is the detector area, Δf is the electrical bandwidth and ΔV_n is the total noise voltage in frequency bandwidth Δf. The detectivity is a form of area normalized signal-to-noise ratio. The highest measured detectivity of the device in vacuum was 6.6×10^5 cm Hz$^{1/2}$/W at 94.4 Hz with a bias current of 970 nA.

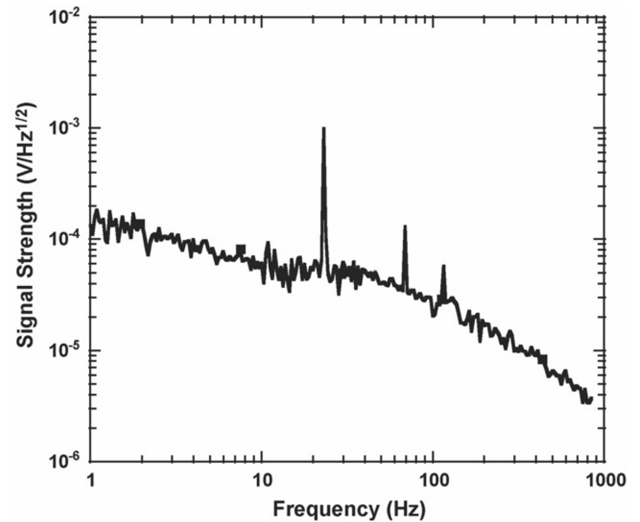

Fig. 5. A typical signal spectrum showing the signal peak at 23 Hz and the noise spectrum. Odd harmonics of the signal are also visible. Measurement was made at 50 mT pressure at a fixed current bias of 970 nA.

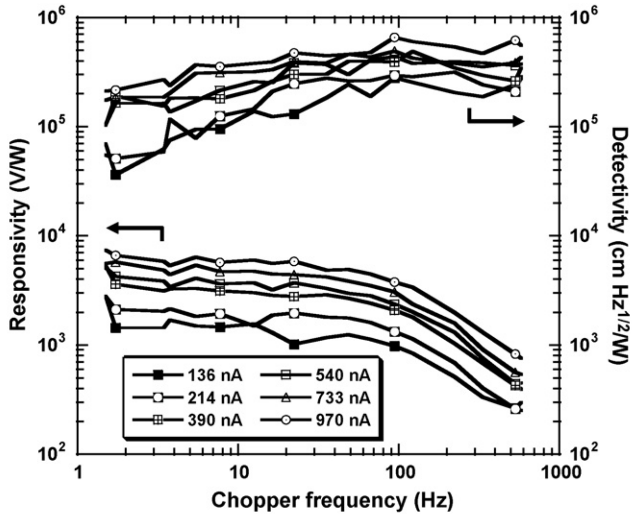

Fig. 6. Responsivity and detectivity in vacuum of a 40 μm × 40 μm detector on a layer of supporting Si_3N_4 vs. optical modulation frequency.

Fig. 6 shows the responsivity and detectivity measured in vacuum as a function of chopper frequency.

The effect of substrate heating on detector performance was also investigated. The detectors were placed in a cryostat with a ZnSe window. The cryostat was evacuated to 50 mT pressure. To emulate a point source, a small aperture was placed in front of the blackbody source and a ZnSe lens was used to focus the infrared energy onto the detector. A smaller aperture would have been desirable as it would have meant higher image resolution. However, the infrared power incident on the detector was a limiting constraint. The aperture was kept at 400–500 μm to keep the power incident on the detector greater than the noise equivalent power (NEP). The lens was mounted on an *XYZ*-axes translational stage controlled by a Newport MM3000 motion controller. This made it possible to traverse a small spot of light on the surface of the detector while keeping the detector in the plane of optical focus. The detector was biased with 0.97 μA of current. An HP 3561A dynamic signal analyzer was used to record the detector output. A SRS 560 low noise amplifier was used to improve the signal to noise ratio before the signal analyzer. The area in the vicinity of the detector was scanned in steps of 25 μm and the detector output signal was plotted using MATLAB. The experiment was performed on two devices; a self-supported 60 μm × 60 μm device [32] and a 40 μm × 40 μm micromachined bolometer supported by a Si_3N_4 membrane presented in this work. The images in Figs. 7 and 8 show a convolution of the spot of infrared light over the area of the detector. The dimensions of the images are comparable to those of the microbolometer pixels. In vacuum environment, the self-supported device is thermally connected

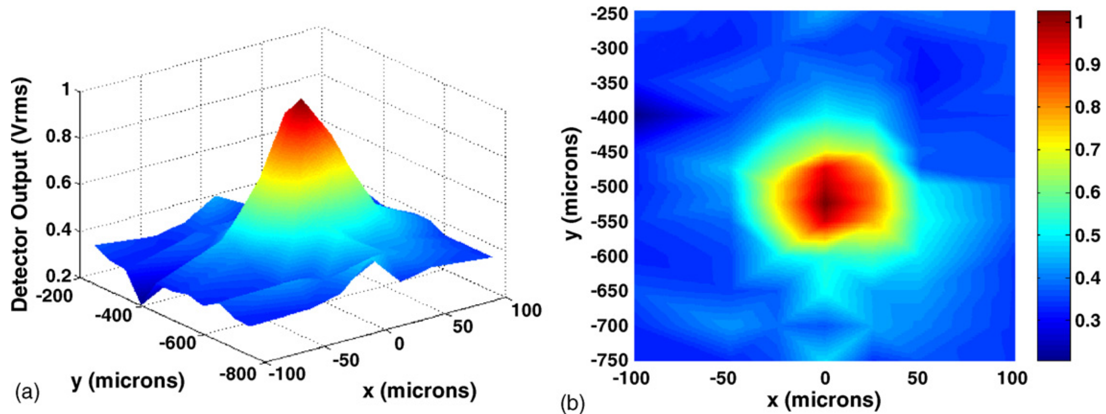

Fig. 7. 60 μm × 60 μm self-supporting device scanned by a point source of infrared light. (a) Isotropic view and (b) top view.

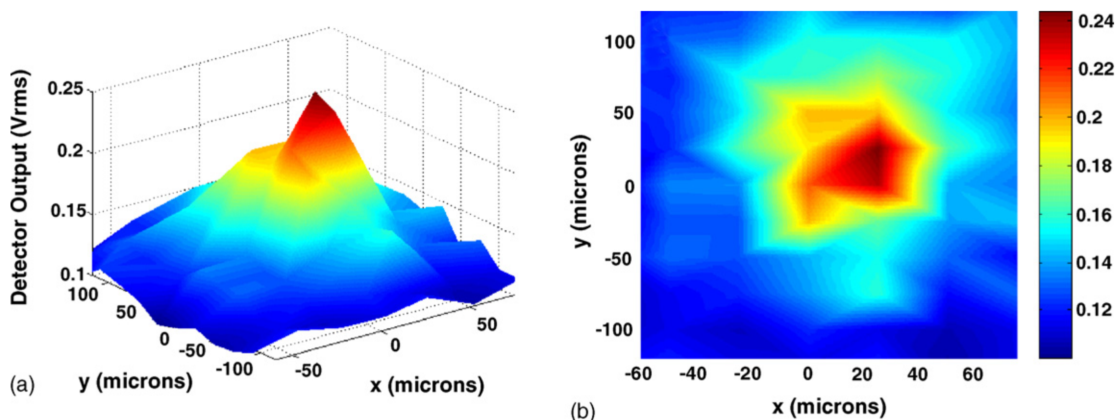

Fig. 8. A 40 μm × 40 μm device on Si_3N_4 support membrane scanned by a point source of infrared light. (a) Isotropic view and (b) top view.

to the ambient by the Ti arms, while the trenches in the supporting Si_3N_4 membrane isolate the detector from the ambient and minimize the effect of substrate heating. Because of good thermal isolation from the ambient, the detectors respond only to direct incident infrared radiation. This makes them suitable candidates for larger arrays on polyimides without compromising image resolution due to cross talk between adjacent pixels.

4. Device-level vacuum packaging

Microbolometers work best when they have as low thermal loss as possible. Isolating the detector from the substrate by micromachining serves to this end. Further improvement in performance is obtained by operation in vacuum. This has hitherto been done by using conventional packaging techniques. The process consists of dicing the wafer, mounting on suitable ceramic or metal packages and wire bonding using ultrasonic or thermo-ionic techniques. This is followed by capping. For microbolometers, this would require an optically transparent cap in the IR range, which can be sealed on top of the package in vacuum. This packaging technique is adopted from traditional CMOS processing, where the packaged chips are mounted on boards for computers and communication devices. This is an expensive technique and also sacrifices the flexibility of the detector.

Chip-scale packaging has also been employed. Of special interest is die-level vacuum packaging technology demonstrated, among others, by Lee et al. [33] and Cheng et al. [34]. The main idea has been to fabricate devices on a silicon wafer and apply a top glass cap structure in vacuum. The joints are sealed to yield vacuum-packaged devices. These methods have shown to provide sufficiently low level of pressure around the packaged device. However, in case of the detectors on flexible substrates, the polyimide substrate has to be peeled off the carrier silicon substrate after completion of the fabrication process, a procedure that would get more challenging with the introduction of a capping wafer. Hence, device-level vacuum packaging is considered.

Using the current microbolometer design, a new device-level packaging scheme was investigated, where the vacuum packaging is completed during the fabrication process, using a combination of conventional micromachining and vacuum sealing techniques. The process builds on the micromachined devices presented above and is fully CMOS compatible. After fabricating the detector pixel, trenches are opened in the supporting nitride layer to expose the underlying sacrificial polyimide (Fig. 1(e)). Instead of proceeding with the micromachining, however, 1 μm-thick photo definable polyimide PI2737 is spun on the wafer and patterned to form a mesa above the detector. Si_3N_4 is then deposited on and patterned to be etched above the polyimide mesa. 0.5 μm of PI2737 is again spun on and patterned to make a larger mesa than the previous one. Another layer of Si_3N_4 (0.5 μm) is deposited and patterned to be removed above the larger mesa. These steps facilitate the fabrication of a stepped nitride well filled with polyimide. A layer of a mechanically strong, albeit optically transparent material, can then be deposited. Slits can be opened in the optical layer to expose the

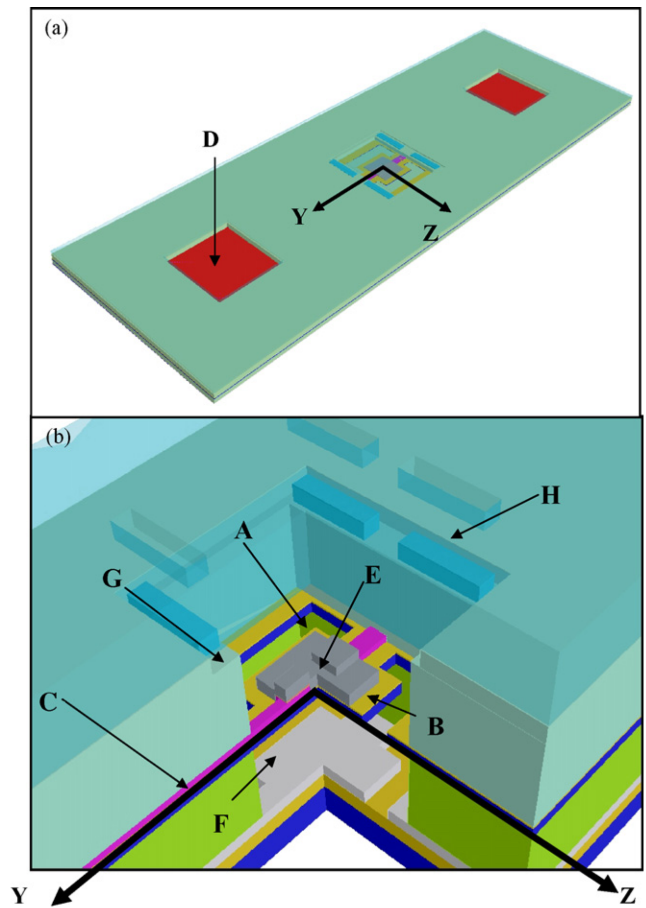

Fig. 9. CoventorWare® model of proposed device-level vacuum packaged microbolometer. (a) Complete bolometer showing open Au bond pads with optical layer rendered transparent and (b) vacuum cavity sectioned at YZ and magnified 20X to show detail. (A) Trench in support layer of Si_3N_4 and $SrTiO_3$ to facilitate micromachining under the bolometer, (B) support layers of Si_3N_4 and $SrTiO_3$, (C) Ti arm, (D) Au pad, (E) YBCO detector element, (F) Al reflecting mirror, (G) lateral etch stop and step geometry to facilitate cavity formation above the detector, (H) optically transparent layer of Al_2O_3 and plugs to seal the vacuum cavity.

sacrificial polyimide that can then be removed by oxygen plasma ashing. The nitride enclosure will limit lateral ashing and direct the micromachining through the open trenches towards the sacrificial polyimide supporting the detector from underneath. Upon completion of the micromachining process, the slits opened in the optical layer can be sealed shut by sputtering some more of the same material. This yields a vacuum cavity evacuated to the sputtering pressure of 10 m Torr and encapsulated by an optical window. Polyimide PI5878G can then be spun onto the wafer to yield the superstrate. The polyimide superstrate provides mechanical strength to the vacuum cavity. It will also help keep the detector close to the zero-strain plane [27]. Bond pads can be opened for subsequent characterization. Fig. 9(a) shows a computer-generated model of the completed vacuum cavity while the interior details of the proposed vacuum cavity can be seen in Fig. 9(b). Given the glass transition temperatures of 400 °C and 360 °C of PI5878G and PI2610 polyimides, respectively, the detectors could be baked at a suitable lower temperature prior to vacuum sealing. This would reduce outgassing

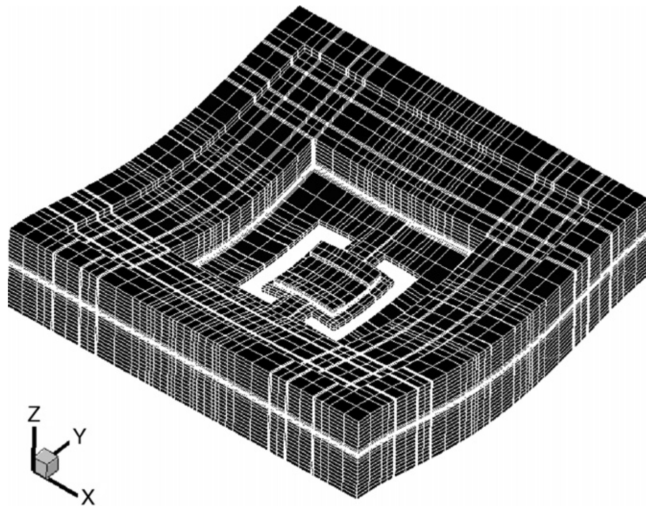

Fig. 10. CoventorWARE® model of a flexible vacuum cavity showing mesh generated for finite-element structural analysis. The figure has been magnified 50X along the *z*-axis and the superstrate and optical window have been removed to show interior details of the cavity.

in the vacuum cavity without affecting the stoichometry of the sensor material YBCO. The impact of baking on the quality of the vacuum over an extended period of time would need to be investigated.

The design of the vacuum cavity will largely depend on the optical and mechanical properties of the material chosen to form the optical window. The optical window will have to withstand a pressure differential of approximately 1 atm. For the vacuum cavity to survive when subjected to the atmospheric pressure and the weight of the superstrate polyimide, the stresses induced on this window should be less than the yield stress of the material. This was investigated using computer simulations. A model of the vacuum package was created using CoventorWare® and analyzed to study feasibility (Figs. 9 and 10). CoventorWare® creates a 3-D model using 2-D process masks and a process flow based on deposit and etch steps. It employs finite-element analysis for numerical computations.

Fig. 10 shows a CoventorWare® model of a flexible microcavity. The polyimide superstrate and the optical window have been removed to show interior details of the microcavity. Based on the mechanical strength and optical transmission characteristics, materials suitable for the role of the optical window include Al_2O_3, ZnSe and Si. Amorphous Al_2O_3 has over 90% optical transmission in the infrared region up to 15 μm [36,37], while ZnSe has an optical transmission range up to 22 μm [36]. Si has an optical transmission range up to 15 μm [36]. All of these materials can be deposited by rf-sputtering. The transmission properties of ZnSe and Si have been quoted for a single crystal material and would be poorer for amorphous films deposited by sputtering. For simulation purposes, the optical window lateral dimensions were kept 100 μm × 100 μm and a thickness of 2.5 μm was assumed. The top surface of the model was exposed to 1 atm pressure. The stress in the optical window was computed using finite-element analysis. Both Al_2O_3 and ZnSe were tested as a window material. It was concluded that Al_2O_3 is the more appropriate material as the stresses developed were less than the tensile strength of 0.26 GPa [36]. The stress in the Al_2O_3 increases as the detector/vacuum cavity is bent across smaller radii of curvature. After application of the superstrate polyimide though, it is the polyimide superstrate and not the Al_2O_3 membrane that maintains the integrity of the vacuum element. Stresses produced in the optical window are shown in Table 1. Similar analysis with a ZnSe optical window showed a failure of the optical window because crystalline ZnSe has much lower yield strength of 55 MPa [38].

Table 1
Induced Von Mises stress in bent microcavity optical window made of Al_2O_3

Radius of curvature (mm)	Max Mises stress (MPa)
48.0	30
12.0	44
7.0	990
5.1	1300
4.2	1500
3.6	1600
3.2	1800
2.9	2000
2.6	2100

Al_2O_3 has a tensile strength of 260 MPa [36].

The optical transmission characteristics of the superstrate polyimide PI5878G have been measured and published [39]. There are transmission windows in the short wave region up to 5 μm as well as another transmission window in the far infrared region around 11 μm. The bolometer needs to be tuned to one of these transmission windows for maximum absorption.

5. Conclusion

A new micromachined infrared detector on a flexible substrate is presented. Unlike previously reported microbolometers on polyimides, these detectors are supported by a thin layer of Si_3N_4. Despite the difference in geometry, the measured thermal conductance G_{th} is comparable to that of self-supported devices. This opens the possibility of employing infrared sensors on thin membranes integrated with pressure sensors or microphones/speakers; thus leading to more compact multi-functional sensor systems on flexible substrates. Room temperature TCR of $-2.63\%\ K^{-1}$ and a relatively low mean thermal conductivity of 5.61×10^{-7} W/K were measured. The maximum responsivity of the detectors was 7.4×10^3 V/W in vacuum. The maximum detectivity in vacuum was $6.6 \times 10^5\ cm\ Hz^{1/2}/W$. The effect of substrate heating on the performance of the detector was also investigated and was found to be negligible. As a step towards truly flexible detectors, the idea of a flexible device-level vacuum cavity was analyzed using FEM based CoventorWARE®. Different materials were simulated to investigate suitability as a robust yet optically transparent optical window material for a self-packaged flexible bolometer. Al_2O_3 was found to be the most suitable. The stresses produced in the vacuum cavity, especially in the optical window, were found to be in the linear region, even when the cavity was bent through a radius of ∼10 mm; mimicking wrapping these detectors around a small cylinder, such as a pen. Future work entails fabrication of vacuum encap-

sulated detectors based on the current analysis. The detectors are going to be sandwiched between a PI5878G superstrate and substrate, creating a vacuum "bubble" around the detectors. This will contribute to greater mechanical strength as the device can be placed in a near-zero-strain plane between the top and bottom layers of the polyimide.

Acknowledgments

This work is based in part upon the work supported by the National Science Foundation under Grants ECS-0401148, and ECS-0245612 and by Semiconductor Research Corporation under Grant 2004-RJ-1271G.

References

[1] S. Mathews, Thermal imaging on the rise, Laser Focus World 40 (2004) 105–107.
[2] W. Radford, D. Murphy, M. Ray, S. Propst, A. Kennedy, J. Kojiro, J. Woolayaw, K. Soch, R. Coda, G. Lung, E. Moody, D. Gleichman, S. Baur, 320 × 240 silicon microbolometer uncooled IRFPAs with on-chip offset correction, SPIE Proc. 2746 (1996) 82–92.
[3] B.E. Cole, R.E. Higashi, R.A. Wood, Monolithic arrays of micromachined pixels for infrared application Tech. Digest, in: IEEE Int. Electron Devices Meet, San Francisco, CA, USA, December 6–9, 1998, pp. 459–462.
[4] T. Breen, N. Butler, M. Kohin, C.A. Marshall, R. Murphy, T. Parker, R. Silva, More applications of uncooled microbolometer sensors, SPIE Proc. 3436 (1998) 530–540.
[5] B. Meyer, R. Cannata, A. Stout, A. Gin, P. Taylor, Amber's uncooled microbolometer LWIR camera, SPIE Proc. 2746 (1996) 13–22.
[6] P.W. Kruse, D.D. Skatrud, Uncooled Infrared Imaging Arrays and Systems, Semiconductors and Semimetals, Academic Press, New York, 1997, pp. 43–121.
[7] R.A. Wood, Use of Vanadium Oxide in microbolometer sensors, Patent No. 5450053 (1993).
[8] R.A. Wood, Use of Vanadium Oxide in microbolometer sensors, Patent No. Re.36615 (1997).
[9] R.E. Higashi, Thermal sensor and method of making same, Patent No. 6144285 (2000).
[10] N.R. Butler, Ambient temperature IR focal plane arrays, SPIE Proc. 4028 (2000) 58–65.
[11] J. Brady, T. Schimert, D. Ratcliff, R. Gooch, B. Ritchey, P. McCardel, K. Rachels, S. Ropson, M. Wand, M. Weinstein, J. Wynn, Advances in amorphous silicon uncooled IR systems, SPIE Proc. 3698 (1999) 161–167.
[12] T. Schimert, D. Ratcliff, J. Brady, S. Ropson, R. Gooch, B. Ritchey, P. McCardel, K. Rachels, M. Wand, M. Weinstein, J. Wynn, Low cost, low power uncooled a:Si based micro infrared camera for unattended ground sensor applications, SPIE Proc. 3713 (1999) 101–111.
[13] C. Vedel, J.-L. Martin, J.-L. Ouvrier-Buffet, J.-L. Tissot, M. Vilain, J.-L. Yon, Amorphous silicon based uncooled microbolometer IRFPA, SPIE Proc. 3698 (1999) 276–283.
[14] W. Radford, R. Wyles, J. Wyles, J. Varesi, M. Ray, D.F. Murphy, A. Kennedy, A. Finch, E.A. Moody, F. Cheung, R. Coda, S. Baur, Microbolometer uncooled infrared camera with 20 mK NETD, SPIE Proc. 3436 (1998) 636–646.
[15] S. Sedky, P. Fiorini, K. Baert, L. Hermans, R. Mertens, Characterization and optimization of infrared poly SiGe bolometers, IEEE Trans. Electron. Dev. 46 (4) (1999) 675–682.
[16] M.S. Liu, J.S. Haviland, C.J. Yue, Integrated Infrared Sensitive Bolometers, Patent No. US005260225A (1992).
[17] P. Fiorini, S. Sedky, M. Caymax, C. Baert, Method of fabrication of an infrared radiation detector and infrared detector device, Patent No. US009194722B1 (2001).
[18] J. Wauters, Doped silicon creates new bolometer material, Laser Focus World 33 (1997) 145–148.
[19] A. Tanaka, S. Matsumoto, N. Tsukamoto, S. Itoh, T. Endoh, A. Nakazato, Y. Kumazawa, M. Hijikawa, H. Gotoh, T. Tanaka, N. Teranishi, Silicon IC process compatible bolometer infrared focal plane array, Tech. Digest, in: International Conference on Solid-State Sensors and Actuators and Eurosensors IX, vol. 2, Stockholm, Sweden, June 25–29, 1995, pp. 632–635.
[20] M.V.S. Ramakrishna, G. Karunasiri, U. Sridhar, G. Chen, Performance of titanium and amorphous germanium microbolometer infrared detectors, SPIE Proc. 3666 (1999) 415–420.
[21] R.B. Lee III, B.R. Barkstorm, H.C. Bitting, D.A.H. Cormmelynck, J. Paden, D.K. Pandey, K.J. Priestley, G.L. Smith, S. Thomas, K.L. Thornhill, R.S. Wilson, Prelaunch calibrations of the Clouds and the Earth's Radiant Energy System (CERES) tropical rainfall measuring mission and Earth Observing System morning (EOS-AM1) spacecraft thermistor bolometer sensors, IEEE Trans. Geosci. Remote Sens. 36 (4) (1998) 117–1185.
[22] P. Eriksson, J.Y. Andersson, G. Stemme, Thermal characterization of surface-micromachined silicon nitride membranes for thermal infrared detectors, J. Microelectromech. Syst. 6 (1) (1997) 55–61.
[23] J.-S. Shie, Y.-M. Chen, M.O-. Yang, B.C.S. Chou, Characterization and modeling of metal-film microbolometer, J. Microelectromech. Syst. 5 (4) (1996) 298–306.
[24] P.C. Shan, Z. Celik-Butler, D.P. Butler, A. Jahanzeb, Semiconducting YBaCuO thin films for uncooled infrared bolometers, J. Appl. Phys. 78 (12) (1995) 7334–7339.
[25] P.C. Shan, Z. Celik-Butler, D.P. Butler, A. Jahanzeb, C.M. Travers, W. Kula, R. Sobolewski, Investigation of semiconducting YBaCuO thin films: a new room temperature bolometer, J. Appl. Phys. 80 (12) (1996) 7118–7123.
[26] A. Yaradanakul, D.P. Butler, Z. Çelik-Butler, Uncooled infrared microbolometers on a flexible substrate, IEEE Trans. Electron. Dev. 49 (5) (2002) 930–933.
[27] A. Yildiz, Z. Çelik-Butler, D.P. Butler, Microbolometers on a flexible substrate for infrared detection, IEEE Sens. J. 4 (1) (2004) 112–117.
[28] C.M. Travers, A. Jahanzeb, D.B. Butler, Z. Çelik-Butler, Fabrication of semiconducting YBaCuO surface-micromachined bolometer arrays, J. Microelectromech. Syst. 6 (3) (1997) 271–276.
[29] A. Jahanzeb, C.M. Travers, Z. Çelik-Butler, D.P. Butler, S.G. Tan, A semiconductor YBaCuO microbolometer for room temperature IR imaging, IEEE Trans. Electron. Dev. 44 (10) (1997) 1795–1801.
[30] J.E. Gray, Z. Çelik-Butler, D.P. Butler, MgO sacrificial layer for micromachining uncooled Y-B-Cu-O IR microbolometers on Si_3N_4 bridges, IEEE J. Microelectromech. Syst. 8 (2) (1999) 192–199.
[31] M. Almasri, D.P. Butler, Z. Çelik-Butler, Self-supporting uncooled infrared microbolometers with low-thermal mass, IEEE/ASME J. Microelectromech. Syst. 10 (3) (2001) 469–476.
[32] S.A. Dayeh, D.P. Butler, Z. Çelik-Butler, Micromachined infrared bolometers on flexible polyimide substrates, Sens. Actuators A 118 (2005) 49–56.
[33] B. Lee, S. Seok, K. Chun, A study on wafer level vacuum packaging for MEMS devices, J. Micromech. Microeng. 13 (2003) 663–669.
[34] Y.-T. Cheng, H. Wan-Tai, K. Najafi, C.T.-C. Nguyen, L. Lin, Vacuum packaging technology using localized aluminum/silicon-to-glass bonding, IEEE/ASME J. Microelectromech. Syst. 11 (5) (2002) 556–565.
[35] E.L. Dereniak, G.D. Boreman, Infrared Detectors and Systems, John Wiley & Sons, Inc., New York, 1996, pp. 407–413.
[36] J.F. Shackelford, W. Alexander (Eds.), CRC Materials Science and Engineering Handbook, third ed., CRC press, Boca Raton, 2001.
[37] M. Aguilar-Frutis, M. Garcia, C. Falcony, G. Plesch, S. Jimenez-Sandoval, A study of the dielectric characteristics of aluminum oxide thin films deposited by spray pyrolysis from $Al(acac)_3$, Thin Solid Films 389 (1–2) (2001) 200–206.
[38] Zinc Selenide Product Data, Crystran Ltd., Poole, Dorset, UK. http://www.crystran.co.uk/products.asp?productid=217.
[39] A. Mahmood, A. Dave, Z. Celik-Butler, D. Butler, Wafer-level self-packaged infrared microsensors, SPIE Proc. 5406 (2004) 473–482.